NANO · MICRO small
www.small-journal.com

Observation of Remote Electroconvection and Inert-Cation Concentration Valley within Supporting Electrolytes in a Microfluidic-Based Electrochemical Device

*Peng Huo, Bingrui Xu, Zhibo Gu, Mingzhuo Su, Shmuel. M. Rubinstein, and Daosheng Deng**

The electrochemical system is playing an increasingly important role in the advanced technology development for drinkable water and energy storage. While the binary electrolyte has been widely studied, such as the associated intriguing interfacial instabilities, multi-component electrolyte is by far less known. Here, based on the classic Cu|$CuSO_4$|Cu electrochemical system, the effect of supporting electrolyte is systematically investigated by highlighting the inert cations. In an annulus microfluidic device, the suppression of a previously known electro-osmotic instability and the emergence of an array of the remote electroconvection along the azimuthal direction is found. A distinctive inert-cation concentration valley propagates radially outward at a speed limited by the electromigration velocity. Remarkably, the simultaneous visualization of spatiotemporal evolution demonstrates the correlation of the concentration valley and electroconvection at a microscopic level. The underlying physical mechanism of their correlation is discussed, and the scaling analysis agrees with experiments. This work might inspire more future work on the multi-component electrolyte, such as for the suppression of interfacial hydrodynamic instability and mitigation of dendrite growth, with the technological implications for water treatment and energy storage in batteries.

1. Introduction

The electrochemical system is essential for the development of the advanced technologies for various applications, such as electrodialysis, desalination, and energy storage in batteries.[1–4] Physically, in the classic Cu|electrolyte|Cu system, rich intriguing interfacial instabilities are exhibited such as morphologic and hydrodynamic instabilities.[5–7] Typically, for a binary electrolyte, the cations can be either chemically reactive or inert with the copper electrodes.[5] For the former case of the reactive cations (such as Cu^{2+} in $CuSO_4$), at a dilute or moderate concentration, the Rubinstein–Zaltzman electroosmotic instability (EOI) due to the extended space charge results in the vortices at the cathode;[8,9] while at a concentrated concentration, the electrodeposition ($Cu^{2+}+2e^- \rightarrow Cu$) leads to the subsequent dendrite growth at the cathode.[10,11] For the latter case of the inert cations (such as Na^+ in Na_2SO_4), in order to sustain the ionic currents, electrolysis of water or water splitting leads to the generation of the bubbles at the cathode ($2H^++2e^- \rightarrow H_2$).[12–14]

In order to control these interfacial instabilities in the binary electrolyte, several approaches have been utilized to regulate either EOI or dendrite growth. EOI can be modified by the surface topology of the ion-selective interfaces or the inhomogeneities in their electrochemical properties,[15] or by introducing the polymer additives against the extensional motion to alter the flow structures.[16] The dendrite growth can be manipulated by decorating the surface charge with polyelectrolyte coatings in the nanopores,[17] by immobilizing a fraction of anions within the electrolyte to reduce the electric field at the metal electrode.[18] Additionally, through a forced convection in the cross-flow, the delayed EOI reduces the dendrite growth in microfluidics.[19]

In this work, in a microfluidic-based Cu|$CuSO_4$|Cu system, the supporting electrolyte is systematically investigated by highlighting the role of inert cations for the first time in experiments. In an annular microchannel, we find suppression of EOI and emergence of an array of the remote electroconvection (REC) along the azimuthal direction. A distinctive inert-cation concentration valley propagates radially outward at a speed limited by electromigration velocity. The simultaneous visualization of spatiotemporal evolution demonstrates the correlation of the concentration valley and vortices at a microscopic level. The underlying physical mechanism is discussed for the formation of the inert-cation concentration valley and the subsequent generation of the transient REC.

P. Huo, B. Xu, Z. Gu, M. Su, D. Deng
Department of Aeronautics and Astronautics
Fudan University
Shanghai 200433, China
E-mail: dsdeng@fudan.edu.cn
B. Xu
Department of Basic Courses
Naval University of Engineering
Wuhan, Hubei 430033, China
S. M. Rubinstein
The Racah Institute of Physics
The Hebrew University of Jerusalem
Givat Ram, Jerusalem 91904, Israel
The ORCID identification number(s) for the author(s) of this article can be found under https://doi.org/10.1002/smll.202108037.

DOI: 10.1002/smll.202108037

Additionally, the phase diagram of various instabilities is established depending on the concentration of working and supporting electrolyte. Scaling analysis provides insight into these observations and agrees with experiments well.

2. Results and Discussion

2.1. REC along the Azimuthal Direction

As shown in the sketch of **Figure 1**a, the polydimethylsiloxane (PDMS) device has a circular microchannel (the thickness h = 30 μm), the cathode is the central copper wire (the inner radius r = 100 μm), and the anode is the outer copper ring (the outer radius R = 3 mm).[20] For the primary working electrolyte of 1 mM $CuSO_4$, the previously well-studied EOI and the associated vortices are observed at the inner cathode at 5 V (Figure 1b,c at t = 18 s, Movie S1, Supporting Information).[8,9,20]

However, by adding the secondary supporting electrolyte of 0.9 mM Na_2SO_4, EOI at the central cathode is suppressed, while an array of REC or the remote vortices along the azimuthal direction emerges in the bulk region away from the electrodes (Figure 1e,f at t = 39 s, Movie S2, Supporting Information). The typical velocity and vorticity for EOI and REC is on the same order of 30 μm s^{-1}, and 0.3 s^{-1} from particle image velocimetry (Figure 1d at t = 2.5 s and Figure 1g at t = 33 s).

The spatial-temporal evolution of REC is presented in **Figure 2**a. During the initial stage until 39 s, no flow or vortex is observed near the cathode. At t_{occ} = 39 s, an array of strong vortices becomes more visible at R_{vortex} ≈ 2 mm away from the inner cathode, and the size of each vortex is about 50 μm. Different from EOI, this REC is transient and lasts for a period with lifetime τ_{life} ≈ 100 s, then gradually disappears after 2 min. Afterward REC gradually fades away, then flow becomes weaker and eventually disappears.

The transition from EOI to REC is determined by the supporting concentration [$c(Na_2SO_4) > c_{cri}$] [Correction added after publication 5 May 2022: the preceding concentration was corrected] (Figure 2b). For the given 1 mM $CuSO_4$ under 5 V, a critical concentration value c_{cri} ≈ 0.4 mM. At the lower concentration [$c(Na_2SO_4) < c_{cri}$], EOI near the cathode is observed as expected. But at the higher concentration [$c(Na_2SO_4) > c_{cri}$] [Correction added after publication 5 May 2022: the preceding concentration was corrected], an array of REC emerges along the azimuthal direction. Once REC is formed, τ_{life} around 100 s and R_{vortex} around 2 mm are nearly insensitive to the concentration.

Furthermore, we survey the different combination of the working and supporting electrolyte at 5 V. For example, REC is observed in $CuCl_2$ (1 mM) - NaCl (0.9 mM), but EOI exists in $CuSO_4$ (1 mM)-$CuCl_2$ (0.9 mM) (Figure 2c). From **Table 1**, the anions (such as Cl^-, $NO\overline{3}$, SO_4^{2-}) are likely irrelevant for REC or EOI. The inert cation (Na^+ or K^+) in the supporting electrolyte is necessary for REC (Figure S2, Supporting Information). REC is not limited in this annulus microchannel, and can be found in more general geometries or setups, such as the microchannels devices with the parallel electrodes (Figure S4, Supporting Information). Hence the presence of the inert cations is arguably accountable for the suppression of EOI and appearance of REC. Once $c(Na_2SO_4) > c_{cri}$, the inert cations of the supporting electrolyte might destroy or demolish the extended space charge in working electrolyte ($CuSO_4$) responsible for EOI,[9] in such a fashion that EOI at the cathode is suppressed.

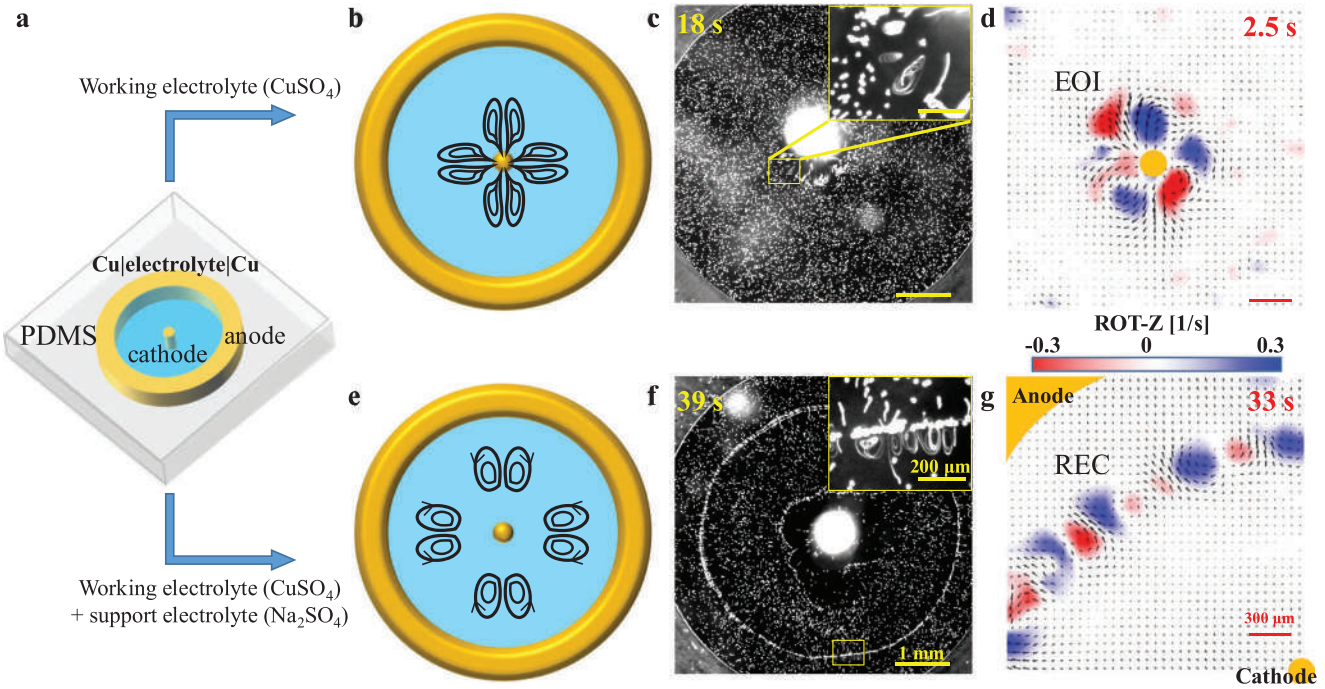

Figure 1. Electro-osmotic instability at the cathode and remote electroconvection in Cu|electrolyte|Cu system. a) Sketch of an annular microfluid device. b,e) Schematic diagram, c,f) the snapshots at 5 V, and d,g) particle image velocimetry for EOI at cathode in the working electrolyte of $CuSO_4$ (1 mM) only, and REC in $CuSO_4$ (1 mM)-Na_2SO_4 (0.9 mM) with the supporting electrolyte.

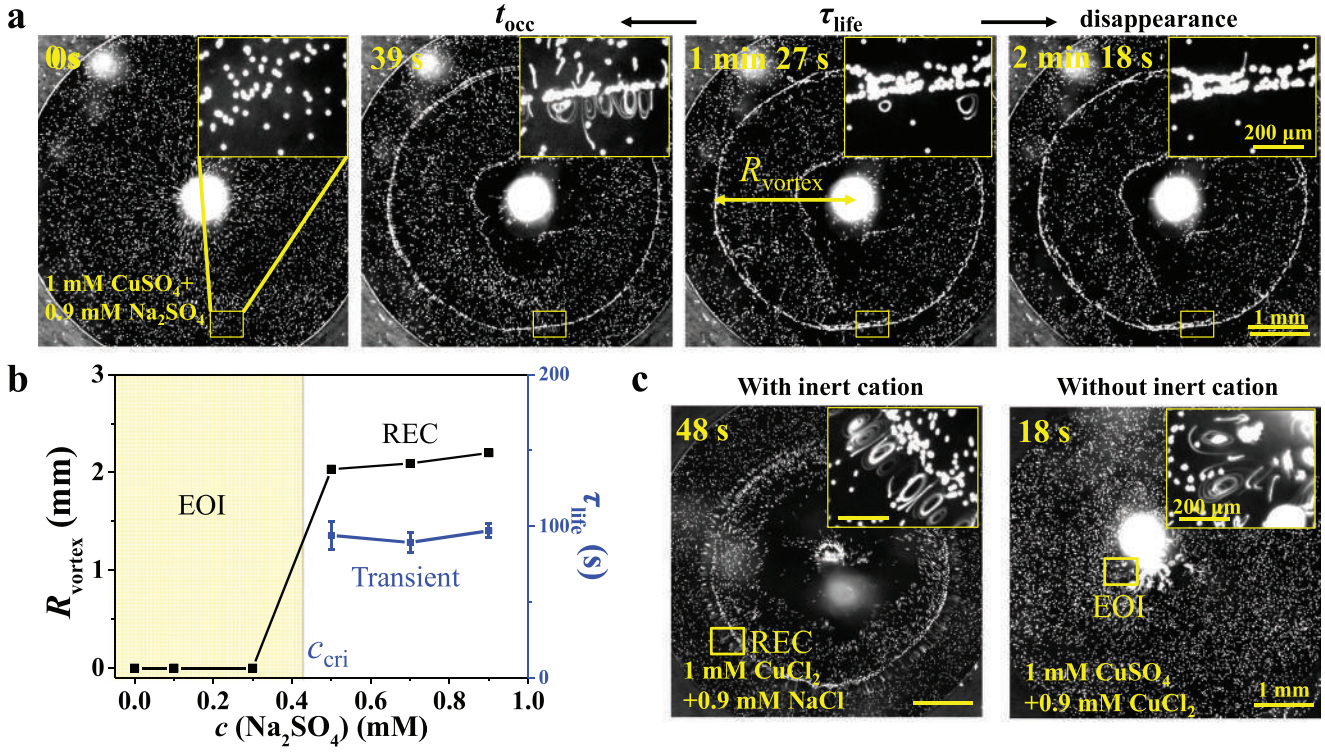

Figure 2. Emergence of REC along the azimuthal direction. a) The spatial-temporal evolution of remote vortices in $CuSO_4$ (1 mM)- Na_2SO_4 (0.9 mM) at 5 V, R_{vortex} for its location and the inner brighter area for the central cathode. b) REC for $c(Na_2SO_4) > c_{cri}$ and the associated R_{vortex} and τ_{life}. c) REC in $CuCl_2$ (1 mM) - NaCl (0.9 mM), and EOI in $CuSO_4$ (1 mM)-$CuCl_2$ (0.9 mM).

2.2. Radial Propagation of Inert-Cation Concentration Valley

In order to reveal the essential role of the inert cations for the emergence of REC, we choose Rhodamine 6G (Rh6G, Rh^+Cl^--type molecule, a highly fluorescent rhodamine family dye with molecular weight about 480) as the supporting electrolyte, since the fluorescent intensity of fluorophore Rh^+ increases with its concentration for the direct visualization. **Figure 3**a shows the spatiotemporal evolution of the fluorescent intensity of Rh^+ in 0.2 mM $CuSO_4$-0.2 mM Rh6G electrolyte at 5 V (Movie S3, Supporting Information). At the beginning, a darker front has a nearly well-preserved circular contours (marked by the red dashed circular lines) and propagates outward radically until 45 s. This darker front corresponds to a lower fluorescent intensity or the local reduction of the inert cations Rh^+. But this circular front or interface is gradually deformed likely arising from the REC, and eventually becomes more complicated at 2 min.

Quantitatively, during the initial period of 45 s, the time-dependent radial profile of Rh^+ concentration or the associated fluorescent intensity (Figure 3b) clearly presents this concentration valley with a local concentration reduction or dip, as marked by R_{valley}. The fluorescent intensity at R_{valley} decreases with time, demonstrating that the concentration at the valley is further reduced. As shown by the time-dependent R_{valley} in Figure 3c, concentration valley propagates outward radially with a constant velocity ($v_{valley} \approx 40\,\mu m\ s^{-1}$) until 35 s. At later stage, the velocity is slowed down as REC occurs.

In order to understand the observed concentration valley of the inert cations, the transport of inert cations (such as Rh^+ or Na^+) is considered carefully (Figure 3d). The reactive cations (Cu^{2+}) of the working electrolyte are directly deposited onto the copper cathode, forming its concentration depletion near the cathode. In contrast, the inert cations subjected to the electric field are migrated toward the cathode, then are charged into the electric double layer (EDL), causing the consequent accumulation or pileup of inert cations in the EDL near the cathode.

The scaling analysis is performed to compare the charging timescale of charging at the (EDL) ($\tau_{charging}$) with migration timescale from bulk to the cathode ($\tau_{migration}$). $\tau_{charging}$ is that for the vanishing of the flux of the inert cations in the entire

Table 1. Combination of working and supporting electrolyte, indicating the inert cations (Na^+ and K^+) necessary for the remote electroconvection (REC).

Working electrolyte	Supporting electrolyte	Reactive cations	Inert cations	REC
$CuSO_4$	–	Cu^{2+}	–	No
$CuSO_4$	$CuCl_2$	Cu^{2+}	–	No
$CuSO_4$	$Cu(NO_3)_2$	Cu^{2+}	–	No
$CuCl_2$	–	Cu^{2+}	–	No
$CuSO_4$	Na_2SO_4	Cu^{2+}	Na^+	Yes
$CuSO_4$	NaCl	Cu^{2+}	Na^+	Yes
$CuSO_4$	KCl	Cu^{2+}	K^+	Yes
$CuCl_2$	NaCl	Cu^{2+}	Na^+	Yes

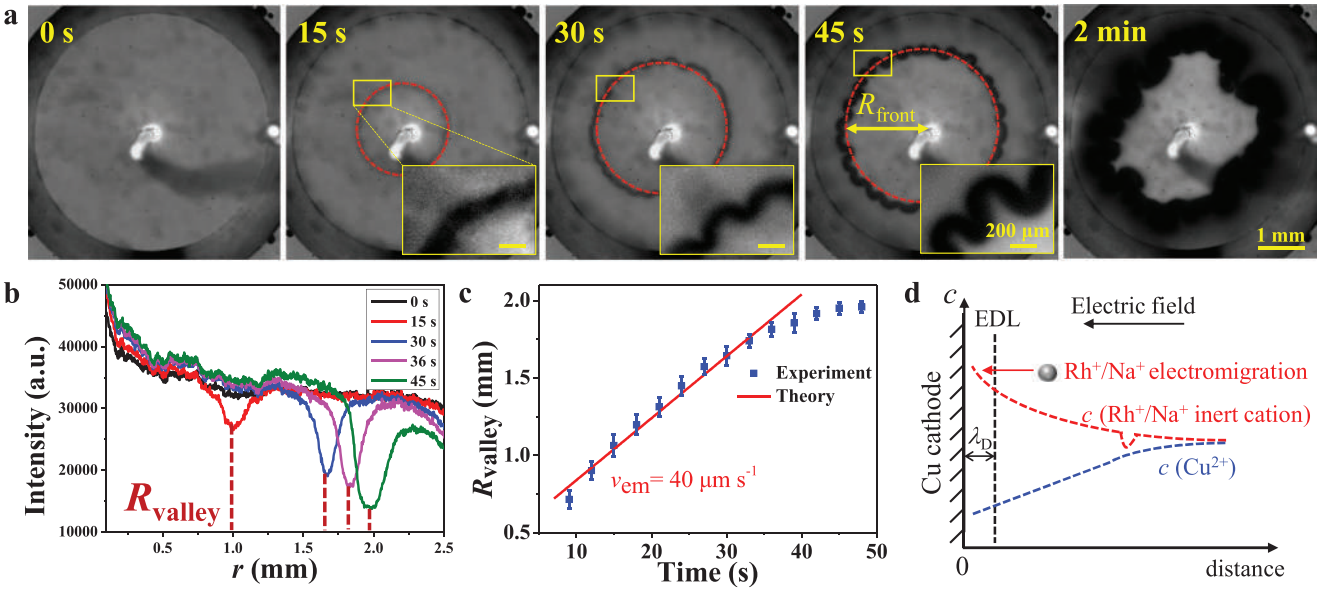

Figure 3. Inert-cation concentration valley propagating radially outward in an aqueous $CuSO_4$-Rh6G. a) Spatiotemporal evolution of the inert-cation Rh^+ fluorescent intensity, the propagation front with a nearly well- preserved circular contour in red until 45 s. Interface being subjected to the deformation and becoming more complicated at 2 min. b) The radial profile of the fluorescent intensity, indicating a pronounced concentration valley with a local dip at R_{valley}. c) Propagation of R_{valley} at an electromigration-limited velocity ($v_{em} \approx 40\,\mu m\ s^{-1}$) initially until 35 s, and gradually slowing down afterward. Error bars for three experiments. d) Sketch of charging into EDL near cathode and electromigration under the electric field for the inert cations (Na^+ or Rh^+).

macroscopic region and is characterized by resistor-capacitor time constant, $\tau_{charging} \sim Res_{inert}Cap$. Here $Res_{inert} \sim 1/c(\text{inert})$ is the resistance for the inert cations, and $Cap \sim \varepsilon/\lambda_D$ is capacitor of the EDL (λ_D for the Debye length, and ε for the dielectric constant).[21] In the multi-component electrolyte, $\lambda_D = \left[\varepsilon k_B T/\sum_i \nu_i (z_i e)^2 c_0\right]^{1/2} \sim c_0^{-1/2}$ depends on the stoichiometric coefficient (ν_i) of the total salt concentration (c_0). Then under the approximation of $c_0 \sim c(Cu^{2+})$ since $CuSO_4$ is the working electrolyte,

$$\tau_{charging} \sim c_0^{1/2}/c(\text{inert}) \sim c(Cu^{2+})^{1/2}/c(\text{inert}) \quad (1)$$

The typical electromigration velocity v_{em} is expressed as below

$$v_{em} = ze\mu E = ze\mu V/L \sim \mu V \quad (2)$$

where $\mu = D/k_B T$ is the Einstein relationship for the ionic mobility, and L, V for the length and the voltage. $\tau_{migration}$ for the inert cations is associated with its migration flux density [$F(\text{inert}) \approx c(\text{inert})v_{em}$]

$$\tau_{migration} \sim c(\text{inert})/F(\text{inert}) \sim 1/\mu V \sim \text{const} \quad (3)$$

Physically, when $\tau_{charging} < \tau_{migration}$, the charging time scale is so fast that the inert cations have insufficient time to supply or transport through migration, subsequently resulting the local dip of concentration. By combining Equations (1) and (3), a critical concentration of inert cations (c_{cri}) is attained above which the concentration valley is formed

$$c(\text{inert}) > c_{cri},\ c_{cri} = \alpha c(Cu^{2+})^{1/2} \quad (4)$$

where α is a coefficient. The existence of a threshold c_{cri} for inert cations (Na^+) to produce the concentration valley is possibly associated with the observed REC [$c(Na^+) > c_{cri}$] (Figure 2b).

Moreover, for the inert cations (Rh^+), from the typical value of diffusivity $D \approx 10^{-9}$ m^2 s^{-1} and electric field $E \approx 10^3$ V m^{-1} (several voltages and several millimeters for the length scale here), the electromigration velocity from Equation (2) is obtained $v_{em} \approx 40\,\mu m\ s^{-1}$. Indeed, as seen in Figure 3c, concentration valley propagates with a constant velocity in experiments ($v_{valley} \approx 40\,\mu m\ s^{-1}$), thatis,

$$v_{valley} \approx v_{em} \approx 40\,\mu m\,s^{-1}\,(5\,V) \quad (5)$$

Therefore the propagation of concentration valley of the inert cations is limited by the velocity of electromigration, and the formation mechanism of the concentration valley ($\tau_{charging} < \tau_{migration}$) is further verified.

At the late stage after 35 s, v_{valley} gradually becomes slower, since the transport becomes more complicated, as the diffusion and convection from REC might be more relevant in the system. As present in the snapshot at 45 s and 2 min (Figure 3a), the azimuthal symmetry of a smooth circular interface at R_{valley} is broken, which likely arises from the presence of REC.

2.3. Correlation between Concentration Valley and REC

In order to directly reveal the coupling of the concentration valley and REC (**Figure 4**a), we carry out the simultaneous visualization of spatiotemporal evolution for concentration and flow by adding fluorescent particles into the CuSO4 (0.2 mM)-Rh6G (0.2 mM) electrolyte. Since the emission intensity of fluorescent

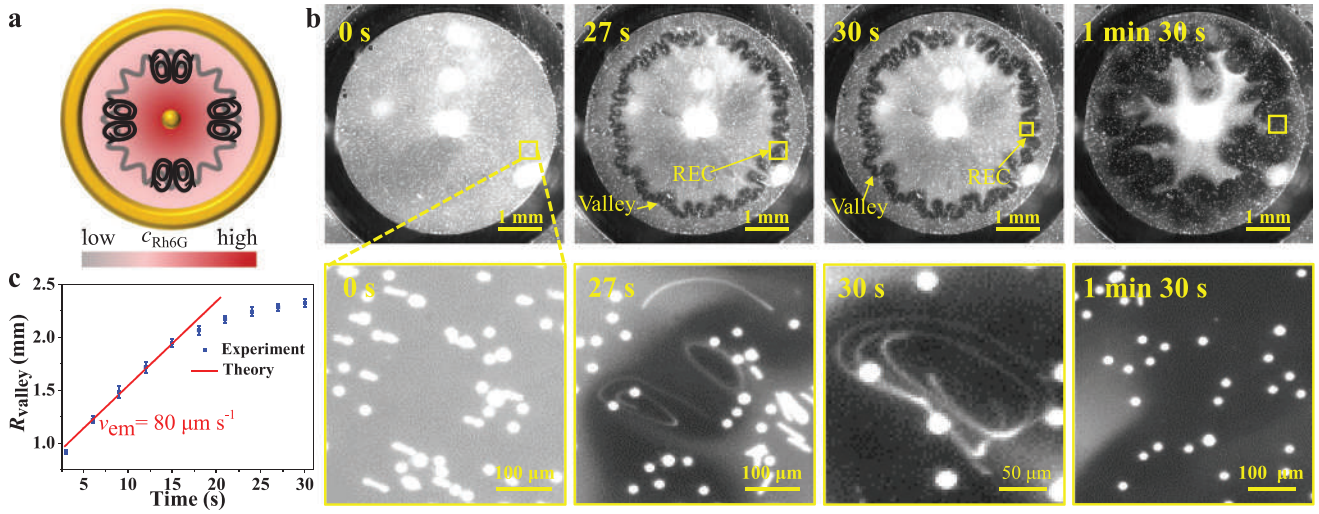

Figure 4. Correlation of the inert-cation concentration valley and REC in an aqueous $CuSO_4$-Rh6G. a) Sketch, and b) snapshot of simultaneous visualization at 10 V, indicating the strong correlation between REC and concentration valley. At $t = 0$ s, uniform concentration in the solution in a steady state. At $t = 27$ and 30 s, obviously REC appearing around the concentration valley, and subsequently causing the deformation of nearly circular interface of propagation front, resulting in more complicated interface. At $t = 90$ s, the interface becomes much more complicated with the azimuthal symmetry broken, and the vortices gradually disappear. The fluorescent intensify for concentration, and the visible path lines for flow. c) Propagation of R_{valley} at an electromigration-limited velocity ($v_{em} \approx 80\,\mu m\ s^{-1}$) during the initial 15 s, and gradually slowing down afterward. Error bars for three experiments.

polystyrene particles is higher than that of Rh6G under the light excitation at wavelength of 559–585 nm, the path lines of particles are more visible to track the flow, while the concentration distribution is obtained simultaneously under the applied voltage at 10 V (Figure 4b; Movie S4, Supporting Information). Again at the initial 30 s, the concentration valley propagates outward while the circular interface is nearly preserved. As the applied voltage is elevated from 5 to 10 V, the estimated electromigration velocity v_{em} from Equation (2), is increased from 40 to 80 μm s^{-1}. Indeed, the time-dependent R_{valley} (Figure 4c) shows a constant propagation speed $v_{valley} \approx 80\,\mu m\ s^{-1}$, again agreeing well with the theory.

$$v_{valley} \approx v_{em} \approx 80\,\mu m\,s^{-1}\,(10\,V) \tag{6}$$

Moreover, by further increasing voltage at 15 and 20 V, v_{valley} is found to excellently agree with the estimated v_{em} as well (Figure S7, Supporting Information), hence further verifying that the propagation speed of the concentration valley is limited by the electromigration velocity.

As shown by the zoom-in view (Figure 4b at t = 27 and 30 s), the size of vortices is around 100 μm, and their location is around the darker region associated with the lower concentration of Rh^+. The propagation front is distorted by the array of remote vortices, and the azimuthal symmetry of the concentration valley indeed is broken. Evidently, their coexistence directly indicates the strong correlation between concentration and REC at the microscopic level.

Similar to the previous studies of the bulk electrokinetic instability,[22–25] the bulk free charge ρ_f in regions of conductivity gradients along the electric field is described by the conservation of the electromigration current and Gauss's law

$$\rho_f = -\varepsilon \mathbf{E}\cdot\frac{\nabla\sigma}{\sigma} \sim \frac{\nabla c}{c} \tag{7}$$

where ε for the permittivity of water. By assuming the continuous or slow spatial variation of the anions and the reactive cations (Cu^{2+}), concentration gradient is mainly derived from the inert cations, such as the observed concentration valley of Rh^+

$$\nabla c \sim \nabla c(\text{inert}) \sim \nabla c(Rh^+) \tag{8}$$

Indeed, the observed concentration valley of inert cations is characterized by a sharp concentration gradient around R_{valley}, generating the bulk free charge.

Experimental realization of the simultaneous visualization of concentration and flow shows that the strong correlation of REC and concentration valley, elucidating the underlying physical mechanism. Here the rapid charging of inert cations into EDL leads to the local concentration dip or minimum of inert cations, and this concentration valley propagates at an electromigration-limited velocity (v_{em}). Meanwhile, the concentration gradient of inert cations [∇c(inert cations)] at the valley is substantially increased, resulting in the free charge in bulk (ρ_f). The net charge under the non-uniform electric field leads to the instability or an array of the vortices for REC.[22–25]

At a late stage, the presented vortices at R_{valley} (Figure 4b at t = 27 and 30 s) can slow down the propagation front and deform the circular front into a much more complicated interface. Also vortices will mix or stir up concentration, reduce the concentration gradient around the concentration valley, and decrease the bulk charge, consequently leading to the eventual disappearance of vortices (Figure 4b at t = 90 s). Finally, once in a certain steady state after sufficiently long period, from the argument of the net zero flux of inert cations $F(Rh^+) = 0$ by balancing the electromigration and diffusion ($Ec \sim D\nabla c$), the inert concentration should decrease monotonously away from the cathode, and the concentration valley shall be diminished accordingly.

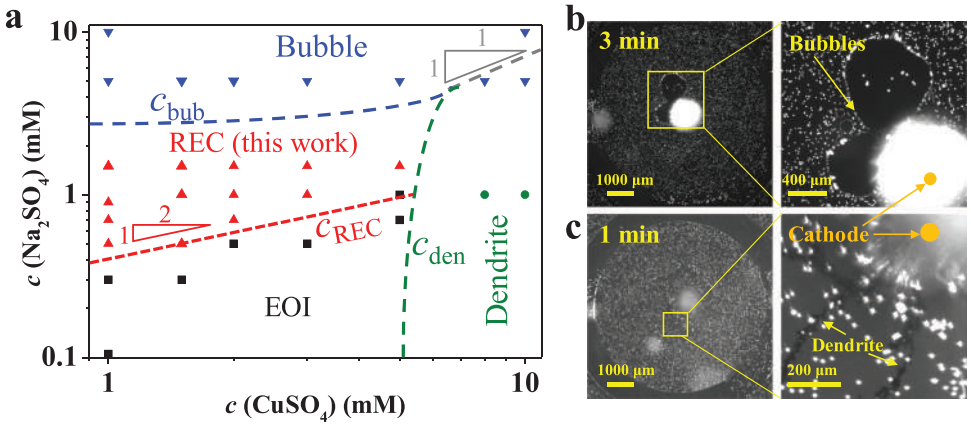

Figure 5. Phase diagram in $CuSO_4$-Na_2SO_4 electrolyte at 5 V. a) Diverse instability depending on the concentration of working and supporting electrolyte, and the 1/2 power law of scaling analysis [$c(Na^+) \sim c(Cu^{2+})^{1/2}$] consistent with the transition between EOI and REC b,c) for the typical images of bubbles in the $CuSO_4$ (1 mM)- Na_2SO_4 (10 mM) solution, and dendrite growth in the $CuSO_4$ (10 mM)- Na_2SO_4 (1 mM) solution, respectively.

2.4. Phase Diagram

For the working electrolyte of $CuSO_4$ at a moderate concentration (such as 1 mM), once $c(Na_2SO_4) > c_{cri}$ (Figure 2b), EOI at the cathode interface is suppressed, while the transient REC is generated away from the electrodes is produced, which is correlated with the propagation of the inert-cation concentration valley. In order to characterize its distinctive difference with EOI, this phase is simplified to be referred to as REC. Dependent on the concentration of working and supporting electrolyte, the different instabilities might take place, and the phase diagram of $CuSO_4$-Na_2SO_4 electrolyte at 5 V is constructed (**Figure 5**a). For a low $c(Na_2SO_4)$ and $c(CuSO_4)$, EOI is generated due to the extended spatial charge at the cathode. For a high $c(Na_2SO_4)$, such as $CuSO_4$ (1 mM)- Na_2SO_4 (10 mM), bubbles are produced by water splitting at the cathodes to sustain the current (Figure 5b). For a low $c(Na_2SO_4)$ and high $c(CuSO_4)$, such as the $CuSO_4$ (10 mM)- Na_2SO_4 (1 mM), Cu^{2+} ions might dominate the ion transport in a way that their fast deposition leads to the dendrite growth[31](Figure 5c). For an intermediate $c(Na_2SO_4)$ and low $c(CuSO_4)$, REC is formed.

To understand the transition among these instabilities, we perform the scaling analysis by comparing their onset timescale. The relevant timescale for EOI is Sand's time (τ_{Sand}), which is required for the concentration of reactive cations (Cu^{2+}) to approach zero at the cathode.[26] τ_{Sand} is expressed in terms of concentration (c), diffusion coefficient (D), and current density ($j \approx Dc_0/L$),

$$\tau_{Sand} \sim Dc_0^2/j^2 \sim L^2/D \sim \text{const} \tag{9}$$

Then τ_{Sand} turns out to be a constant, regardless of the concentration. The rate of dendrite growth from the copper ions linearly increase with concentration,[27] and hence the associated timescale is as following

$$\tau_{dendrite} \sim 1/c(Cu^{2+}) \tag{10}$$

Once $c(Cu^{2+})$ reaches above a threshold c_{den} (the green line in Figure 5a), $\tau_{dendrite} < \tau_{Sand}$ and the dendrite growth becomes dominant.

The bubble dynamics including nucleation and growth is much more complicated due to water electrolysis,[14] but its production rate is simply assumed to be proportional with the available sodium ions, so the timescale of bubble is as below,

$$\tau_{bubble} \sim 1/c(Na^+) \tag{11}$$

Once $c(Na^+)$ increases beyond a threshold c_{bubble} (the blue line in Figure 5a), $\tau_{bubble} < \tau_{Sand}$, the bubbles are produced.

The transition between the dendrite growth and bubble formation is obtained

$$\tau_{dendrite} \sim \tau_{bubble}, c(Cu^{2+}) \sim c(Na^+) \tag{12}$$

This linear scaling of $c(Cu^{2+}) \sim c(Na^+)$ (the gray line in Figure 5a) is comparable with the experimental data.

The transition from EOI to REC is associated with the presence of inert-cation concentration valley, the following scaling is identified by comparing charging and transport of inert cations from Equations (1) and (3),

$$\tau_{charging} \sim \tau_{migration}, c(Na^+) \sim c(Cu^{2+})^{1/2} \tag{13}$$

This 1/2 scaling is consistent with the experiments (the red line in Figure 5a). Hence, the scaling analysis provides the theoretical guidance for the transition of these instabilities in the experiments.

2.5. Discussion and Outlook

Several topics are briefly outlined to be investigated in future as below:

i) By adding the supporting electrolyte, the well-studied Rubinstein–Zaltzman EOI at the interface is suppressed experimentally. In a recent study of non-binary electrolyte containing a mixture of three species (polymeric ink-containing particles and positively and negatively charged ions),[29] EOI still exists although its onset might be modified.

A simple 1D ternary model by considering the three ion species (the reactive cations and inert cations, and the anions) might shed light on the spatial-temporal evolution of their concentration. A quantitative and rigorous numerical simulation is desirable by resolving EDL deliberately ($\lambda_D \sim$ nm and the bulk length scale approximately~mm), in order to address the vanishing of extended space charge, the formation of the concentration valley for inert cations and the consequent flow instability.

ii) Since REC is correlated with the inert-cation concentration valley in experiments, the bulk charge from the concentration gradient is proposed to be responsible for the observed flow.[22,23,25] The surface charges and the associated nonuniform electro-osmotic flows along the walls might affect the vortices as well since the height of the microchannel is only around 30 μm.[25,30] By modifying PDMS surface from negative to positive charges through the surface treatment, REC is nearly unaffected experimentally. But the interplay of free charge and surface charge together with the flow might be clearly resolved in numerical simulation.

iii) Different from the previous study for the dendrite growth in the concentrated $CuSO_4$ with presented Na_2SO_4,[31,32] here we focus on the effect of the supporting electrolyte (Na_2SO_4) on EOI at the moderate concentration of 1 mM $CuSO_4$ (Figure 5a), and find the suppression of EOI and emergence of REC once [$c(Na_2SO_4) > c_{cri}$]. Nevertheless, the effect of the inert cations on the dynamics and morphology of dendrite growth needs to be further explored systematically, likely leading to the possible mitigation of dendrite growth at the electrochemical interface.[19,33]

iv) The inert cations of supporting electrolyte in the simple Cu|$CuSO_4$|Cu model has been shown to significantly influence the ion transport and produce REC in both the annulus microchannels and the straight microchannels with parallel electrodes. The inert cations might be anticipated to be crucial in other more complicated setups and geometries, including the practical electrochemical system for diverse applications, such as the electrodialysis for water treatment and energy storage in the batteries.

3. Conclusion

In summary, in the classic Cu|$CuSO_4$|Cu electrochemical system, we systematically investigate the multi-component electrolyte by highlighting the significant role of inert cations in the supporting electrolyte for the first time. In $CuSO_4$-Na_2SO_4, we find the suppression of the well-studied EOI by the supporting electrolyte and an emergence of array of REC along the azimuthal direction [$c(Na_2SO_4) > c_{cri}$]. In $CuSO_4$-Rh6G electrolyte, the direct visualization of spatiotemporal evolution of the inert cations reveals that a distinctive inert-cation concentration valley propagates radially outward at an electromigration-limited speed (v_{em}). The correlation of the concentration valley and vortices at a microscopic level is demonstrated by the simultaneous visualization of their spatiotemporal evolution at the microscopic level. The underlying physical mechanism is discussed for the formation of the inert-cation concentration valley and the subsequent generation of REC arising from the bulk charge. Scaling analysis provides insight into these observations and agrees with experiments well. Specifically, 1/2 scaling [$c(Na^+) \sim c(Cu^{2+})^{1/2}$] for the transition from EOI to REC is consistent with the phase diagram dependent on the concentration of working and supporting electrolyte. These results would be expected to inspire more future work in the multi-component electrolyte with the relevant technological implications for water treatment and energy storage in batteries, such as suppression of interfacial hydrodynamic instability and mitigation of dendrite growth.

4. Experimental Section

PDMS Device: The microchannel was fabricated with PDMS (Sylgard 184, Dow corning) on a pattern produced by photolithography. The microchannel was sealed with a flat PDMS plate via plasma treatment. To modify the surface charge, the PDMS surface was treated by the air plasma, and then was immersed into the poly(allylamine hydrochloride) (PAH) solution (5 mg mL^{-1} PAH with 0.5 M NaCl) to generate positive surface. The solution was injected into the channel through the syringe pump, and a constant voltage was applied by Keithley 2450 Source Meter.

Visualization of Flow: For flow visualization, the injected solution in the microchannel was mixed with fluorescent polystyrene particles (0.01% solids, the diameter 3.2 μm, Invitrogen) to visualize vortices by the fluorescent microscope (Zeiss, Axio Zoom V16) together with Tween80 (0.1 wt%, Sigma Aldrich) to avoid particles aggregation.[20]

Visualization of Concentration: For concentration visualization, Rh6G (Sigma Aldrich) as a highly fluorescent rhodamine family dye is a Rh^+Cl^--type molecule, and the inert cation Rh^+ (molecular weight about 443) as the fluorophore allowed the direct concentration visualization. Indeed the intensity of fluorescence increased with the concentration of Rh^+, or vice versa from the calibration (Figure S5a, Supporting Information); and its fluorescence intensity was unaffected by neither the copper cation (Cu^{2+}) nor the *p*H (Figure S5b,c, Supporting Information). The spatiotemporal evolution of the fluorescent intensity in 0.2 mM $CuSO_4$-0.2 mM Rh6G electrolyte was captured by the fluorescent microscope (Zeiss, Axio Zoom V16) with an exposure time of 3 s.

Simultaneous Visualization of Flow and Concentration: For simultaneous visualization of flow and concentration, fluorescent particles (0.01 % solids, 3 μm) were added into the $CuSO_4$ (0.2 mM)-Rh6G (0.2 mM) electrolyte. Since the emission intensity of fluorescent polystyrene particles was higher than that of Rh6G under the light excitation at wavelength of 559–585 nm, the path line of particles was more visible to track the flow, while the concentration distribution was obtained simultaneously, enabling the simultaneous visualization of concentration and flow.

Supporting Information

Supporting Information is available from the Wiley Online Library or from the author.

Acknowledgements

The authors appreciate I. Rubinstein and B. Zaltzman for the idea to study supporting electrolyte and theoretical guidance including the scaling analysis here. D.D. was grateful for the discussion with M. Bazant and J. Santiago. This work was supported by the National Program in China and startup from Fudan University, the China Postdoctoral Science Foundation.

Conflict of Interest

The authors declare no conflict of interest.

Data Availability Statement

The data that support the findings of this study are available from the corresponding author upon reasonable request.

Keywords

concentration valleys, electrochemical systems, electroconvection, inert cations, supporting electrolytes

Received: December 27, 2021
Revised: February 18, 2022
Published online: March 8, 2022

[1] R. F. Probstein, *Physicochemical Hydrodynamics*, Wiley, New York **2003**.
[2] M. A. Shannon, P. W. Bohn, M. Elimelech, J. G. Georgiadis, B. J. Marinas, A. M. Mayes, *Nature* **2008**, *452*, 301.
[3] V. V. Nikonenko, A. V. Kovalenko, M. K. Urtenov, N. D. Pismenskaya, J. Han, P. Sistat, G. Pourcelly, *Desalination* **2014**, *342*, 85.
[4] J. X. Zheng, M. S. Kim, Z. Y. Tu, S. Choudhury, T. Tang, L. A. Archer, *Chem. Soc. Rev.* **2020**, *49*, 2701.
[5] E. Yariv, Y. Almog, *Phys. Rev. Lett.* **2010**, *105*, 176101.
[6] V. R. Stamenkovic, D. Strmcnik, P. P. Lopes, N. M. Markovic, *Nat. Mater.* **2017**, *16*, 57.
[7] D. Fraggedakis, M. Z. Bazant, *J. Chem. Phys.* **2020**, *152*, 184703.
[8] I. Rubinstein, B. Zaltzman, *Phys. Rev. E* **2000**, *62*, 2238.
[9] B. Zaltzman, I. Rubinstein, *J. Fluid Mech.* **2007**, *579*, 173.
[10] R. M. Brady, R. C. Ball, *Nature* **1984**, *309*, 225.
[11] M. Rosso, *Electrochim. Acta* **2007**, *53*, 250.
[12] R. Simons, *Nature* **1979**, *280*, 824.
[13] J. Mo, Z. Kang, S. T. Retterer, D. A. Cullen, T. J. Toops, J. B. Green, M. M. Mench, F. Y. Zhang, *Sci. Adv.* **2016**, *2*, e1600690.
[14] M. Y. Wang, Z. Wang, X. Z. Gong, Z. C. Guo, *Renew. Sustain. Energy Rev.* **2014**, *29*, 573.
[15] S. M. Davidson, M. Wessling, A. Mani, *Sci. Rep.* **2016**, *6*, 22505.
[16] G. J. Li, L. A. Archer, D. L. Koch, *Phys. Rev. Lett.* **2019**, *122*, 124501.
[17] J.-H. Han, E. Khoo, P. Bai, M. Z. Bazant, *Sci. Rep.* **2014**, *4*, 7056.
[18] M. D. Tikekar, L. A. Archer, D. L. Koch, *Sci. Adv.* **2016**, *2*, e1600320.
[19] M. C. Ma, G. J. Li, X. Chen, L. A. Archer, J. Wan, *Sci. Adv.* **2021**, *7*, eabf6941.
[20] Z. B. Gu, B. R. Xu, P. Huo, S. Rubinstein, M. Z. Bazant, D. S. Deng, *Phys. Rev. Fluids* **2019**, *4*, 113701.
[21] M. Z. Bazant, K. Thornton, A. Ajdari, *Phys. Rev. E* **2004**, *70*, 021506.
[22] J. F. Hoburg, J. R. Melcher, *J. Fluid Mech.* **1976**, *73*, 333.
[23] J. D. Posner, J. G. Santiago, *J. Fluid Mech.* **2006**, *555*, 1.
[24] S. J. Kim, S. H. Ko, R. K. Kwak, J. D. Posner, K. H. Kangb, J. Han, *Nanoscale* **2012**, *4*, 7406.
[25] K. Dubey, S. Sanghi, A. Gupta, S. S. Bahga, *J. Fluid Mech.* **2021**, *925*, A14.
[26] P. Bai, J. Li, F. R. Brushetta, M. Z. Bazant, *Energy Environ. Sci.* **2016**, *9*, 3221.
[27] C. P. Nielsen, H. Bruus, *Phys. Rev. E* **2015**, *92*, 052310.
[28] B. R. Xu, Z. B. Gu, W. Liu, P. Huo, Y. T. Zhou, S. M. Rubinstein, M. Z. Bazant, B. Zaltzman, I. Rubinstein, D. S. Deng, *Phys. Rev. Fluids* **2020**, *5*, 091701(R).
[29] A. Ratzabi, T. Eluk, A. Levy, Y. Feldman, *Phys. Rev. Fluids* **2021**, *6*, 113701.
[30] E. V. Dydek, B. Zaltzman, I. Rubinstein, D. S. Deng, A. Mani, M. Z. Bazant, *Phys. Rev. Lett.* **2011**, *107*, 118301.
[31] M. Q. López-Salvans, P. P. Trigueros, S. Vallmitjana, J. Claret, F. Sagués, *Phys. Rev. Lett.* **1996**, *76*, 4062.
[32] F. SaguesFrancésc, M. Q. López-Salvans, J. Claret, *Phys. Rep.* **2000**, *337*, 97.
[33] S. Wei, Z. Cheng, P. Nath, M. D. Tikekar, G. Li, L. A. Archer, *Sci. Adv.* **2018**, *4*, eaao6243.

